Geophys. J. R. astr. Soc. (1982) **68**, 429–458

The 1978 earthquake sequence near Thessaloniki (northern Greece)

C. Soufleris, J. A. Jackson, G. C. P. King and C. P. Spencer *Bullard Laboratories, Department of Earth Sciences, University of Cambridge, Madingley Rise, Madingley Road, Cambridge CB3 0EZ*

C. H. Scholz *Lamont-Doherty Geological Observatory, Palisades, New York 10964, USA*

Received 1981 May 20; in original form 1981 January 21

Summary. This paper presents a detailed study of teleseismically and locally recorded foreshocks and aftershocks of the 1978 Thessaloniki earthquake sequence and discusses the relations between the locations and mechanisms of these shocks and the three-dimensional geometry of faulting in the source region.

Sixteen teleseismically recorded events were relocated using a relative relocation method and positioned geographically using the accurate (locally determined) location of the largest aftershock. All these shocks had depths shallower than 15 km. The spatial distribution of the foreshocks showed that the activity was initiated at the central part of the epicentral region, progressed westwards, and for about 20 days clustered in the region of the imminent mainshock. No teleseismically recorded foreshock was located west of the mainshock location. In less than 1 hr after the mainshock large aftershocks occurred west of it and, in later stages, spanned the entire western part of the epicentral region. No teleseismically recorded aftershocks were located east of the mainshock.

Locally recorded aftershocks were accurately located and provided a more detailed picture of the seismic deformation. They occurred at depths between 3 and 12 km and in three distinct clusters, separated by well-defined gaps.

The largest foreshock, on May 23, had a moment of 5.6×10^{24} dyne cm and a mean displacement of 31 cm. The mainshock, on June 20, had a moment of 5.2×10^{25} dyne cm, a strain drop of 4.0×10^{-5} (static stress drop of 12 bar) and a mean displacement of 64 cm.

These values are for one of the two possible interpretations of the aftershock distribution, which suggests that the largest earthquakes of the sequence occurred on two different, but adjacent, fault segments. The first (Event 1, on May 23) occurred along the central fault segment and was followed

28 days later by the second (Event 2, on June 20) along a western fault segment. Finally, 61 days later another smaller earthquake (Event 3) occurred along another fault, east of Event 1.

1 Introduction

In the spring and summer of 1978 the Thessaloniki region of northern Greece was severely affected by a series of earthquakes, with the largest ($m_b = 6.1$) occurring on June 20. These shocks occurred along faults forming a graben structure at the northern end of the Aegean basin, which is an area undergoing active extension (McKenzie 1978).

Soufleris & Stewart (1981) and Soufleris & King (1981) have reported the relocation of the four largest events of the sequence and used waveform modelling to show that the largest foreshock and the mainshock had depths between 4 and 8 km, which are in agreement with teleseismic relocation results. Another 12 teleseismically recorded events of the sequence are relocated in the present report and their locations are discussed together with the locations of the locally recorded aftershocks.

2 Teleseismic relocations

Routine teleseismic locations are usually in error due to inadequate station coverage, systematic and random reading errors and bias due to the difference between the real Earth and the earth model used in the location. It is difficult to evaluate the contribution of each of the above error sources to the final mislocation. Large earthquakes are usually widely and clearly recorded so that errors due to poor station distribution and misreadings will be reduced. For these shocks the final error may be largely due to the assumed earth model. For smaller events poor station distribution and misreadings will introduce larger errors. A relative relocation scheme reduces the bias due to the assumed earth model.

The relative relocation method of Jackson & Fitch (1979) which uses *P* and *PKP* arrival times was employed here and the 16 largest shocks of the Thessaloniki sequence were relocated. An initial location for the largest event (the mainshock of June 20) was assumed and the other shocks were relocated with respect to it. In this way bias due to the earth model used for the location of the reference mainshock became common to all the events. The pattern was then placed geographically using the accurate location of the largest aftershock, determined by a network of local stations by Carver & Bollinger (1981), thus removing the bias due to the earth model.

Most of the relocated events were small ($5.0 > m_b > 4.4$) and had not been well recorded. It is therefore possible that they lack information regarding certain of their parameters. Such a lack of information is shown by the presence of small eigenvalues of the observation equation matrix and results in large standard error estimates (Crosson 1976; Aki & Lee 1976). The effect of small eigenvalues can be suppressed by using the damped least squares solution (e.g. Crosson 1976) which reduces the standard errors but also decreases the resolution. However, for well-recorded events there should be no significant differences between the damped and undamped solutions. The damped least squares solution was used here and convergence was usually achieved after no more than six iterations. Damping was performed by adding $\theta^2 I$ increments to the diagonal elements of the normal equations matrix ($A^T A$), where $\theta = 1/\sigma_x$. To evaluate the effect of damping on the final solution a range of damping levels was considered. The four basic damping coefficients σ_x were: 0.4 s for the differential origin time, 2 km for the length and 0.25 rad for the azimuth and polar angle of the vector from the master to a secondary. These are typical values of the standard errors, checked by chi-square tests, from the maximum likelihood (or undamped least squares) solutions of

Table 1. Variation in the solution vector, the standard errors and the diagonal elements of the resolution matrix for various levels of damping. The four basic damping coefficients (see text) are multiplied by the damping factor (D.F. in column 1). Note that by increasing the damping factor (i.e. decreasing the damping) the errors become larger and so does the resolution. A resolution near 1 denotes a well-resolved parameter. For large damping factors the undamped solution is obtained. (Length in kilometres, azimuth and polar angle in degrees.)

	Solution vector			St. Errors			Resolution		
D.F.	L	Az	Pol	L	Az	Pol	L	Az	Pol
EVENT 223, No of stations = 240									
1	4.9	131.9	73.4	0.6	7.0	6.1	0.89	0.60	0.38
2	5.1	133.7	89.5	0.7	9.4	13.0	0.97	0.88	0.67
4	5.1	133.8	90.8	0.7	10.3	17.9	0.99	0.97	0.89
10	5.1	133.8	90.8	0.7	10.6	20.0	1.00	0.99	0.98
100	5.1	133.8	90.8	0.7	10.7	20.5	1.00	1.00	1.00
EVENT 204, No of stations = 148									
1	13.2	255.4	87.8	0.7	3.9	5.4	0.84	0.92	0.74
2	12.9	255.1	90.5	0.8	4.3	8.4	0.95	0.98	0.90
4	12.9	255.1	90.6	0.9	4.4	9.7	0.99	0.99	0.97
10	12.9	255.1	90.6	0.9	4.4	10.1	1.00	1.00	1.00
EVENT 312, No of stations = 40									
1	10.7	131.9	61.4	0.9	7.1	5.4	0.54	0.56	0.58
2	11.0	128.9	58.5	1.6	10.7	10.1	0.77	0.83	0.80
4	10.9	123.0	59.4	2.1	12.0	13.4	0.92	0.95	0.94
10	10.9	122.7	59.9	2.3	12.6	15.9	0.99	0.99	0.99
100	10.9	122.7	59.9	2.4	12.7	16.3	1.00	1.00	1.00
EVENT 314, No of stations = 22									
1	11.4	119.5	67.4	0.9	7.0	5.8	0.41	0.50	0.55
2	10.9	123.0	111.4	1.6	12.0	11.2	0.77	0.77	0.49
4	11.9	123.5	122.0	2.5	14.8	20.1	0.84	0.93	0.80
10	12.0	123.5	122.7	3.8	16.3	28.6	0.96	0.99	0.96
100	12.0	123.6	122.8	4.4	16.8	33.4	1.00	1.00	1.00

well-recorded earthquakes. Table 1 shows the solution vector, the standard errors and the diagonal elements of the resolution matrix for four representative events of the sequence. For well-recorded shocks (such as event 223) the solution vector is not significantly affected by variations in damping, but for earthquakes recorded by fewer stations (such as event 314) it may change significantly. Events of the latter type were excluded from the final analysis. A damping factor (D.F. in Table 1) equal to 2 gave well-resolved parameters and acceptable standard errors and was chosen for the final calculation. The location of the mainshock, on June 20, as relocated by Soufleris & Stewart (1981) was taken as the master (or reference) event and the other shocks were relocated with respect to it. Fig. 1 shows the epicentres and Tables 2 and 3 the hypocentral parameters of the relocated shocks after they have been placed geographically using the location for number 16 given by Carver & Bollinger (1981). The activity has been shifted about 8 km south-east of the ISC and USGS locations.

The basic requirement of the relative relocation scheme is that a station can only be used if it has recorded both the master and the secondary events. This reduces the effective number of stations used for each relocation. However, the rms residuals, shown in Table 2, are smaller by a factor of 2 or 3 than those of the ISC or USGS (usually 1 to 2 s) and it appears that the increased accuracy gained by the relative relocation outweighs the effect of the fewer stations provided that a good station coverage is retained. The above locations are likely to be accurate to within about 3–6 km.

The relocated epicentres of the Thessaloniki sequence (Fig. 1) show an east-to-west migration. Evidence for such a migration also exists in the macroseismic data of Comninakis & Papazachos (1979). It is interesting that all the relocated foreshocks in May (numbers 1–4) were east of the mainshock and all but one of the aftershocks were to the west of the

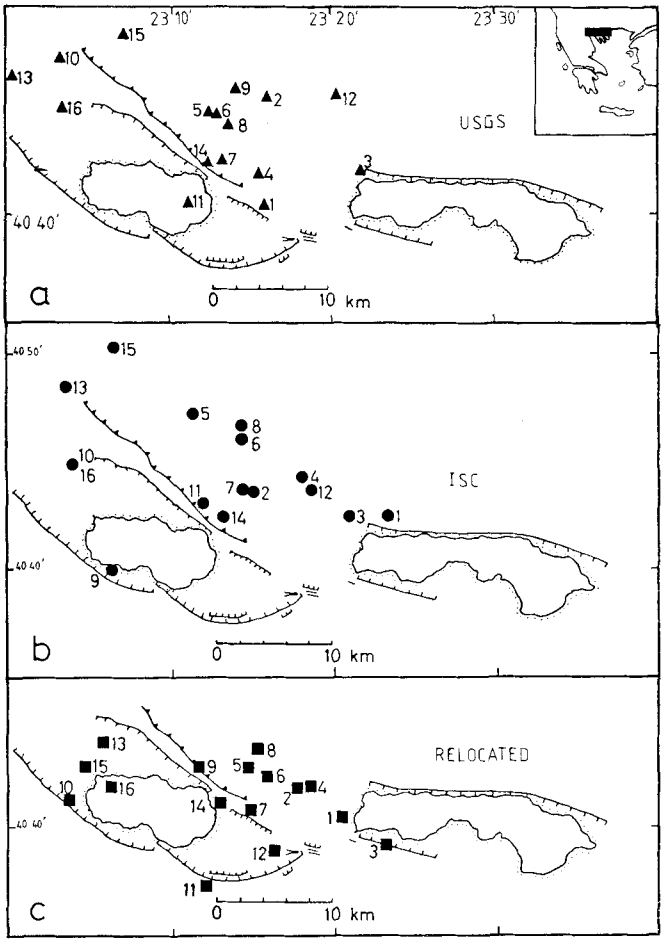

Figure 1. USGS (top), ISC (middle) teleseismic locations and relocated epicentres (bottom) for the 16 largest events of the 1978 sequence. Old normal (hatched) and reverse (teeth) faults are shown without any reference to their age. The 1978 fractures (after Mercier *et al.* 1979) are the short densely hatched normal fault segments between the two lakes. Numbers are sequential and identify events in Tables 2 and 3. Number 8 is the mainshock of June 20. Inset shows the epicentral area of the 1978 sequence.

Table 2. Relocation parameters and the corresponding diagonal elements of the resolution matrix. Azimuth (in degrees), polar angle (in degrees) and distance (in kilometres) of each secondary event are with respect to the master (event 8).

					Resolution matrix			
No	Az	Pol	L	RMS	Or.t	Az	Pol	L
1	128.9	58.5	11.0	0.85	0.88	0.83	0.80	0.77
2	133.7	89.5	5.1	0.63	0.95	0.88	0.67	0.97
3	126.8	65.7	15.2	0.73	0.80	0.95	0.82	0.84
4	127.5	45.6	7.6	0.75	0.85	0.68	0.67	0.68
5	207.7	173.6	16.2	0.59	0.90	0.54	0.97	0.62
6	172.2	35.3	4.4	0.60	0.94	0.74	0.68	0.89
7	186.8	60.1	6.1	0.64	0.92	0.86	0.62	0.86
8			M A S T E R					
9	253.2	30.3	10.6	0.54	0.83	0.68	0.79	0.51
10	255.0	96.6	17.0	0.47	0.67	0.94	0.69	0.74
11	200.9	72.8	13.2	0.68	0.90	0.98	0.87	0.85
12	171.1	143.9	15.1	0.65	0.85	0.89	0.90	0.57
13	272.3	123.9	15.9	0.69	0.90	0.96	0.93	0.85
14	215.2	60.0	6.1	0.66	0.92	0.86	0.55	0.79
15	264.3	113.6	16.2	0.53	0.74	0.93	0.74	0.68
16	255.1	90.5	12.9	0.61	0.92	0.98	0.90	0.95

Table 3. Final hypocentre parameters for the relocated 16 largest events of the sequence. To evaluate the quality of each location the final hypocentre parameters must be viewed together with Table 2. Note that the above error estimates are a measure of internal consistency and provide no indication of the real mislocation errors. Origin time and magnitude are taken from the ISC bulletin.

							St. Errors		
No	Date	Or. t.	Lat.	Lon.	D	m_b	St.	Lat.	Lon.	D
1	08-05-78	143900	40.676	23.341	12	4.4	40	3.0	0.3	1.2
2	23-05-78	233411	40.698	23.295	6	5.6	240	1.0	0.3	1.3
3	24-05-78	021228	40.654	23.385	12	4.8	84	2.7	0.6	2.0
4	24-05-78	055728	40.699	23.305	11	4.7	54	2.5	0.5	0.2
5	02-06-78	223125	40.715	23.244	-10	4.7	115	1.3	0.5	1.9
6	19-06-78	103106	40.707	23.258	10	5.3	205	1.6	0.7	0.1
7	20-06-78	104811	40.681	23.247	9	4.9	87	1.6	1.4	0.9
8	20-06-78	200322	40.729	23.254	6	6.1	385	-	-	-
9	20-06-78	204523	40.715	23.194	15	4.5	31	1.0	2.7	0.2
10	20-06-78	205240	40.690	23.061	4	4.4	25	1.7	1.4	3.3
11	20-06-78	215104	40.623	23.201	10	4.7	91	1.3	1.6	1.8
12	21-06-78	060005	40.650	23.270	-6	4.6	48	0.7	1.4	2.5
13	21-06-78	122943	40.734	23.098	-2	4.8	94	1.3	0.2	2.4
14	21-06-78	185206	40.687	23.215	8	4.5	58	0.7	2.2	1.1
15	23-06-78	015702	40.716	23.079	0	4.2	30	1.8	0.0	3.1
16	04-07-78	222328	40.700	23.106	6	5.0	148	0.8	0.9	2.0

mainshock. There was also a foreshock concentration in June (numbers 5–7) near the mainshock location. Almost all the relocated shocks had depths between 0 and 12 km. Event 9 (an early aftershock, 42 min after the mainshock) was located at a depth of 15 km, but its distance L from the master was not well resolved (Table 2). The same applies for event 12 which was located in the air.

Most of the activity was north-west of the main surface ruptures of 1978 suggesting that the earthquake fault (or faults) dips northwards.

3 Locally recorded aftershocks: instrumentation

During the period July 20 to August 31 a variable number of portable stations were operated locally. Table 4 lists the coordinates of these stations and their period of operation and shows that eight stations were operating for most of the recording period.

The instruments used were all smoked drum recorders (four Lamont type and four Sprengnether MEQ-800) and were coupled with Willmore MK II and Mark Product L4-C vertical component short period (1 Hz) seismometers. The filter settings were adjusted to have a flat frequency response between 1 and 10 Hz. Amplifier gains were set to either 78 or

Table 4. The local recording stations and their period of operation. The latitude and longitude are in degrees and minutes and the height H in metres. The time correction Dt (in s) is the height difference from the lowest station divided by a P-wave velocity of 5.5 km s^{-1}.

Stat.	Lat.	Lon.	H	Dt	Operation Per.
PLA	4038.38N	2321.27E	500	0.08	22 JUL-29 AUG
PRO	4042.44N	2317.37E	300	0.04	20 JUL-29 AUG
KOL	4045.39N	2309.04E	230	0.03	23 JUL-24 AUG
ARD	4036.10N	2310.70E	350	0.05	22 JUL-25 AUG
VAY	4042.91N	2322.96E	140	0.01	25 AUG-29 AUG
TOU	4040.38N	2304.17E	160	0.01	22 JUL-25 AUG
KNI	4044.44N	2323.46E	460	0.07	25 AUG-29 AUG
ASK	4044.83N	2324.97E	540	0.09	22 JUL-13 AUG
REM	4047.36N	2322.41E	500	0.08	13 AUG-29 AUG
VOL	4041.91N	2326.55E	100	0.00	23 JUL-08 AUG, 14 AUG-24 AUG
MIV	4040.98N	2333.93E	100	0.00	08 AUG-14 AUG
LAI	4043.34N	2259.80E	220	0.02	23 JUL-02 AUG
ARE	4046.51N	2315.46E	560	0.09	02 AUG-11 AUG

84 db corresponding to a signal magnification from the ground motion to the trace on the record of 25 000 and 50 000 respectively. The recorders were adjusted to rotate at a speed of 60 mm min^{-1} for the MEQ-800 and 120 mm min^{-1} for the big-drum Lamont instruments, which gave 2-day records for both types. Clock-drifts were checked every two days with a radio time-signal and were always found to be less than 0.05 s over the 2-day period. Time corrections added to the earthquake arrival times were linearly interpolated over the period between two checks. The positions of the stations were determined using topographic maps of 1 : 50 000 scale and are believed to be accurate to within about 300 m.

The acquired data consisted of 150 seismograms, containing more than 12 000 *P*-arrivals in total.

4 Data reduction

Despite the large amount of data it was decided that the analysis would be based on the locations of *all* the locatable events. In similar studies a magnitude cutoff is usually set and only earthquakes above that magnitude are considered. However, this analysis was concerned with the detailed seismic deformation in the source region and even smaller events, reflecting probable internal deformation of blocks, were considered of interest. Thus the cutoff level was defined by the inherent limitations in the data (i.e. events which could not be located because they were only recorded by three stations). In this way a more uniform dataset was secured, complete in the range of local magnitude M_L from -1 to 4. Furthermore, the large number of located events allowed the selection of a large number of high quality locations for the final discussion. The procedure of reading arrival times and other pertinent data for each earthquake was automated with the help of a high resolution (0.025 mm) digitizing table. The automation process included the reading and storing of the arrival time data for each record, the grouping of the arrival times for the same event and the preparation of data for the location program.

With a high resolution digitizer the reading accuracy of *P*- and *S*-phases depends on the accuracy of placing the cursor on the exact position of that arrival. Repeated tests showed that the reading accuracy of a *P*-arrival was consistently 0.1 mm, which corresponds to a time accuracy of 0.1 s for the 60 mm min^{-1} records and to 0.05 s for the 120 mm min^{-1} ones. The reading accuracy for the *S*-arrivals was lower because it was more difficult to pick the exact arrival time of the *S*-phase in the coda of the *P*-wave. However, *S*-phases were usually sharp and distinct in most cases and repeated tests showed that they could be read to within 0.2 s. Based on the above reading accuracies the *S*-arrivals were assigned one-fourth of the weight of the *P*-arrivals for all the locations.

In the next stage the arrival times for each day and for all stations were merged in one dataset and arrivals for the same earthquake were sorted and grouped together. Finally, arrival times and coda duration for each event were set up ready for the location program.

Each station was assigned a time correction for its height difference from the lowest station. This difference was divided by a *P*-wave velocity of 5.5 km s^{-1} which was assumed for the uppermost layer of the crust. Preliminary location tests for a group of well-recorded earthquakes gave station residuals of the order of 0.1 s, close to the reading accuracy of the *P*-arrivals. No station with consistently small or large residuals was found and for this reason no other station corrections were assigned.

The magnitude of each earthquake was estimated from the signal duration of the event T (in s), at each station, using a formula similar to the one of Lee & Lahr (1975) but with different constants:

$$M = C + 3.28 \log T - 0.05\,\Delta$$

where Δ is the epicentral distance (in km) and C is a constant, different for each station (B. Papazachos 1978, private communication). Four large aftershocks recorded by the local network had been assigned local magnitude M_L by the Athens Observatory. These events were used to calibrate the constant C for each station.

All the earthquakes presented here have been located using the HYP071 location program (Lee & Lahr 1975).

5 Velocity structure

Information for a crustal model of the epicentral region is available from Makris & Moller (1977) who carried out a refraction experiment about 30 km to the south. The purpose of that experiment was to determine the thickness of the nearby ophiolites. Their longest refraction line was 30 km and their results showed that the ophiolites are 2.5 km thick and lie on a basement whose P-wave velocity is 6 km s^{-1}.

6 Travel-time curves and V_p/V_s ratio

Travel times of earthquakes contain information about their locations and the velocity structure. In the present section information about the P- and S-wave velocities in the epi-

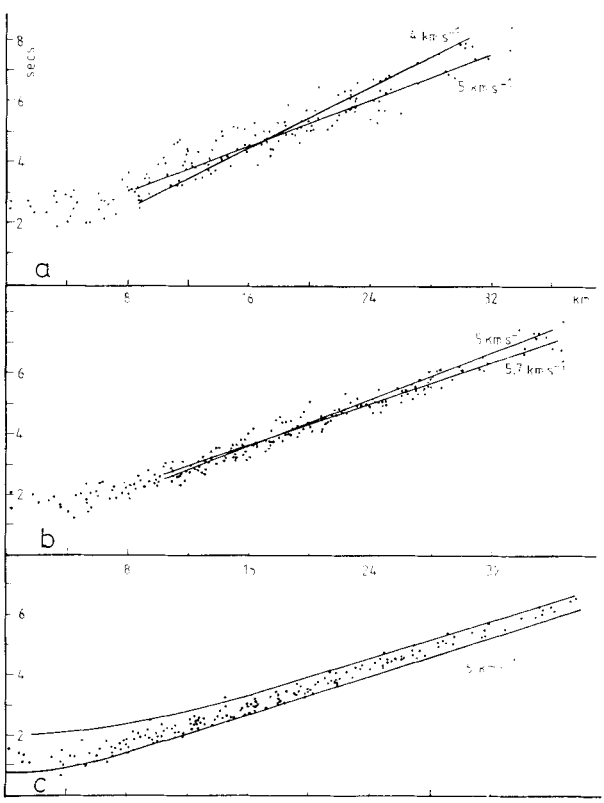

Figure 2. Travel-time curves for well-recorded aftershocks. In (a) and (b) the steeper lines represent velocities used in the location and the shallower lines represent the best straight line fit to the travel times. Fig. 2(c) shows data points and theoretical travel-time curves for depths of 5 and 12 km with a P-wave velocity of 6 km s^{-1}, which was used for both the location and the calculation of the travel-time curves. Note the decrease in scatter from (a) to (c).

central region is extracted from 65 well-recorded events. Each of these events was located using at least seven *P*- and three *S*-arrivals.

A homogeneous half space was taken as the starting model and the 65 events were located for different values of its *P*-wave velocity. Initially, the earthquakes were located with a *P*-wave velocity of 4 km s^{-1} and travel-time curves were plotted (Fig. 2a). The points show a large scatter and the best straight line through them has a slope of 0.2 implying a *P*-wave velocity of 5 km s^{-1}. The new inferred velocity was used for the relocation of the same events and the new travel-time curves are shown in Fig. 2(b). They show a smaller scatter than in Fig. 2(a) and the best straight line through them has a slope of 0.18, implying a new *P*-wave velocity of 5.7 km s^{-1}. The earthquakes were relocated once more using a *P*-wave velocity of 6 km s^{-1} and travel-time curves were again plotted (Fig. 2c). The new points show the least scatter and the best straight line implies a *P*-wave velocity of 6 km s^{-1}. This suggests that a *P*-wave velocity of 6 km s^{-1} is a good estimate of the average *P*-wave velocity in the region and agrees with the results of Makris & Moller (1977).

In the next stage rms travel-time residuals for individual events were examined more carefully to see whether the shallower earthquakes had systematically better locations when

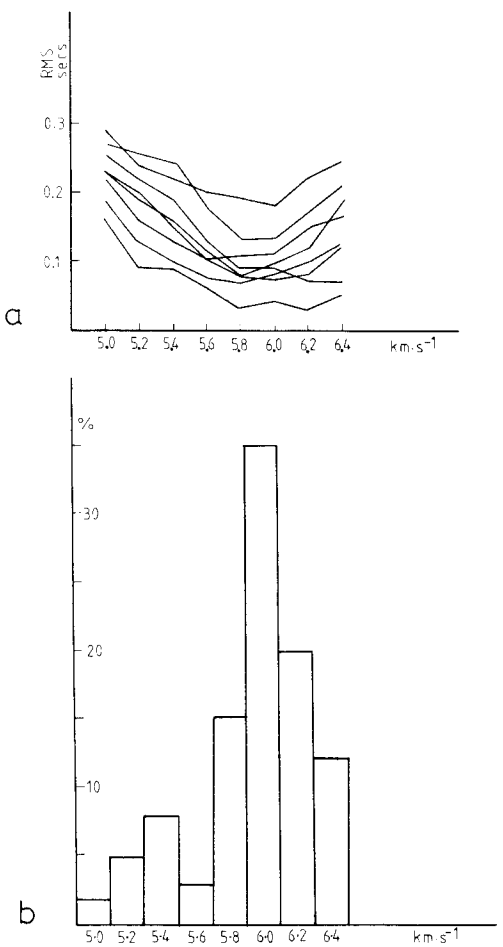

Figure 3. Rms time residuals versus *P*-wave velocities used for the location of selected events (a), and a histogram (b) showing the percentage of events and the velocity which resulted in their minimum rms residual. A total number of 65 events was considered.

P-wave velocities smaller than 6 km s^{-1} were used. No systematic trends were observed and the same velocity of 6 km s^{-1} resulted in the minimum rms time-residuals for shallow and deep events. Some events and their rms residuals are shown in Fig. 3(a). The histogram in Fig. 3(b) was used to calculate a weighted mean *P*-wave velocity of 5.9 km s^{-1}.

The V_p/V_s ratio was calculated using the same 65 well-recorded earthquakes. *P*-wave travel times were plotted against *S* minus *P* travel times (i.e. Wadati plots) and the results showed considerable scatter with no systematic trend. A mean value of 1.82 ± 0.12 was calculated and subsequently used for all the locations.

7 Location accuracy: the effect of the station distribution

Both the network geometry and errors in the data affect the errors of an earthquake location. In this section the uncertainties in the solution vector are calculated from the covariance matrix $C = \sigma^2(A^TA)^{-1}$, where A is the observation equation matrix and σ^2 is the variance in the data as evidenced in the travel-time residuals. The square roots of the four diagonal elements of the covariance matrix are the standard deviations of the four hypocentral parameters (e.g. Jeffreys 1961). Matrix A depends only on the partial derivatives of the travel-time functions and, therefore, is a function of the ray geometry and the velocity structure. The covariance matrix C can be constructed from A, without actually performing the iterative procedure on real data, provided that there is an *a priori* estimate of σ^2 (e.g. Peters & Crosson 1972).

The covariance matrix C was computed for a number of fictitious earthquakes located on a grid covering the entire epicentral region. *P*- and *S*-arrivals were weighted according to the accuracy to which they were read (i.e. the weight of the *P*-arrival is four times the weight of the *S*-arrival). Standard errors in origin time, depth, latitude and longitude were calculated by multiplying the square roots of the diagonal elements of the covariance matrix by $\sigma = 0.15$ s, which is a typical value of the standard deviation of travel-time residuals for good locations in the present dataset. Error contours were subsequently drawn and the effects of various station distributions were determined by comparing the contour maps for various combinations of stations and types of data. Fig. 4 shows results of this test in the form of contour maps for the case where eight stations with two *S*-arrivals were used. Errors in depth are low in the vicinity of the stations, especially for events just outside the network. Similar results were found by Peters & Crosson (1972) and Lilwall & Francis (1978). Errors in depth for the shallower events are larger than for the deeper events. This happens because, for the constant velocity model used here, the partial derivative of the travel time with respect to depth ($\cos i/v$, where i is the ray take-off angle) tends to zero as the free surface is approached. As a result, the column corresponding to depth in the observation equation matrix has near-zero values and the normal equation matrix becomes near-singular, resulting in large depth errors.

Jackson (1980) and Ellsworth & Roecker (1982) found that in order to minimize the errors in depth and origin time, one must seek to maximize the variance of the ray take-off angles. This means that the inclusion of both up- and down-going rays improves the depth resolution. In the one-layer model used here, however, refracted (down-going) rays are prohibited.

In conclusion, it was found that when six, seven or eight stations were used then two *S*-arrivals can ensure location errors of the order of 2 km in epicentre and depth for earthquakes within the area covered by the network or about 6 km outside it. However, when five stations were used then three *S*-arrivals would ensure the same accuracy, and when only four stations were used then both *P*- and *S*-arrivals are required at all stations.

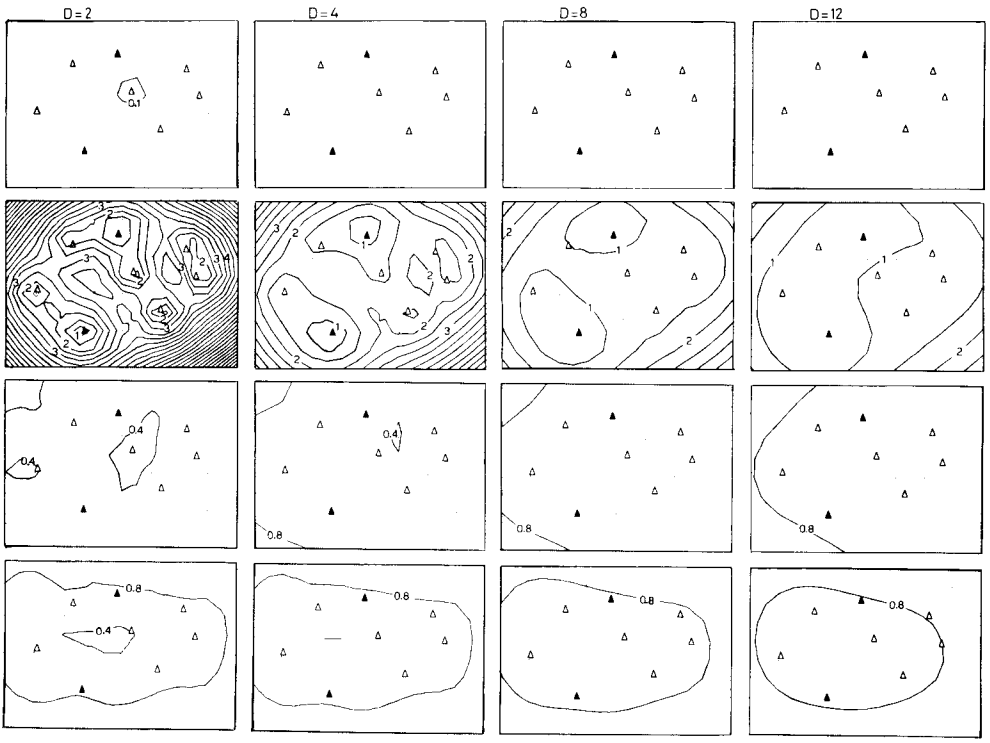

Figure 4. Location error contours in (from top to bottom) origin time (in seconds), depth (in kilometres), longitude (in kilometres) and latitude (in kilometres) for eight *P*- and two *S*-arrivals. The numbers at the top of each column of contour maps denote depth (in kilometres). Stations are shown as triangles (filled if the station reports both *P*- and *S*-arrivals). The bottom left corner of each contour map is at 40° 32′ N, 22° 52′ E and the area covered by each square is 48 × 35 km.

8 The effect of random noise

The location errors described in the previous section were those predicted by the linear theory and it is not certain that the linear approximation holds for all parts of the epicentral region. To test the validity of the linear error estimates additional tests were carried out and fictitious events were relocated after their travel times had been contaminated by random noise.

Travel times to eight stations were calculated for synthetic earthquakes in a homogeneous half space with a *P*-wave velocity of 5.9 km s^{-1} and a V_p/V_s ratio of 1.82. Random noise of a normal distribution, with zero mean and a standard deviation of 0.1 s for *P*- and 0.3 s for *S*-arrivals was added to the travel times and the events were relocated. The difference between the initially assumed location and the relocated position was taken as the mislocation error. The test was carried out for a variety of combinations of *P*- and *S*-arrivals.

In general, the mislocation errors were in good agreement with the errors predicted by the linear theory in the previous section for earthquakes in areas surrounded by the network or 6–10 km outside it.

A test with the standard deviation of the random noise increased to 0.2 s for *P*- and 0.6 s for *S*-arrivals increased the mislocation errors by a factor of 2 for earthquakes inside the network and by a factor of 2–4 for events outside it. In the same test it was also found that the depth resolution decreased and a large number of events were fixed by the location program at 6 km (the starting depth in the computation).

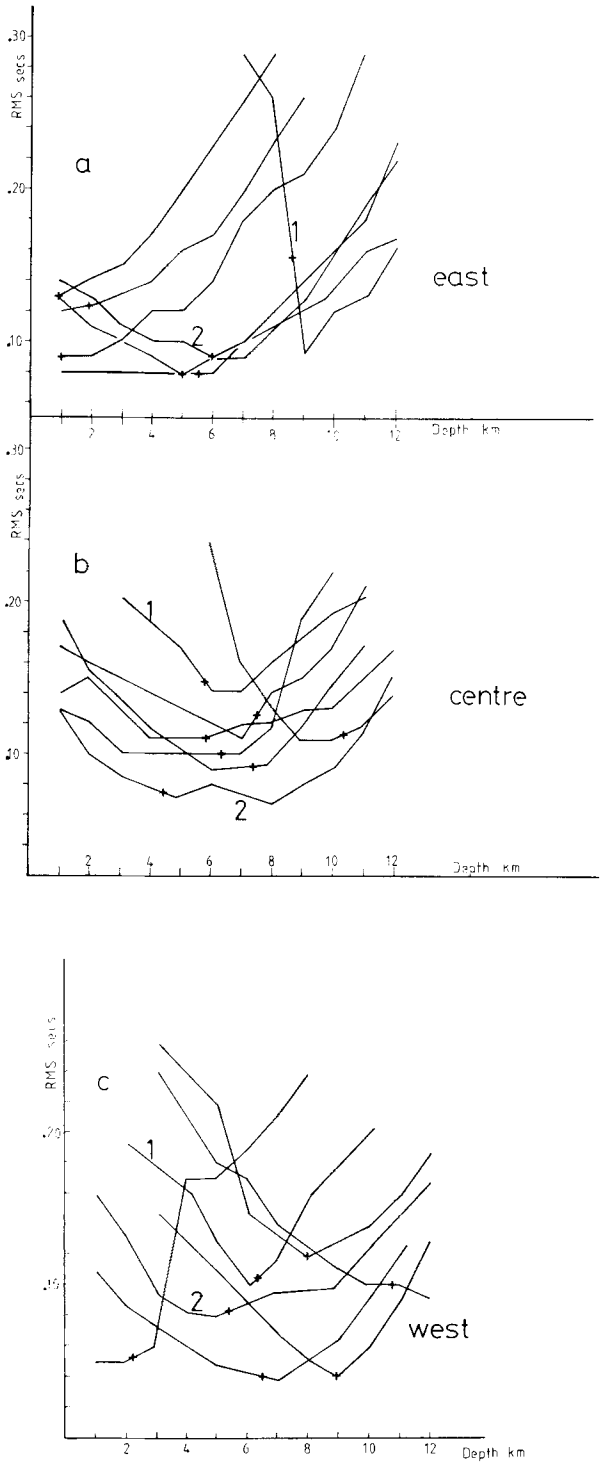

Figure 5. Rms time residuals versus depth for selected real earthquakes in the eastern (a), the central (b) and the western (c) parts of the activity. A cross marks the depth calculated by the free solution. Note that several of the events in the east (a) have minimum rms residuals for shallow depths suggesting that activity there was shallower than the activity in other parts. For further discussion see text.

9 Depth resolution

The final test was concerned with depth resolution only. To examine whether the convergence to the finally computed depth depends on the starting depth, hypothetical earthquakes were repeatedly relocated with the iteration process starting at a different depth. For earthquakes located with *P*-arrivals only it was found that when the initial depth was too shallow (deep) the event was finally located shallower (deeper) than its real position, by amounts generally larger than the linearly predicted error. However, for earthquakes recorded by stations with a good azimuthal distribution and with two or more *S*-phases, the final location was generally close to the real location and within the error limits predicted by the linear theory.

The computation convergence to the final depth was then more closely examined. The HYP071 location program solves for origin time, epicentre and depth by minimizing the sum of the squares of the travel-time residuals. The final hypocentre, therefore, must be at the position where the rms residual is minimum. But is this always the case? To test this a group of real earthquakes was fixed at a certain depth and the program was made to calculate the best origin time and epicentre for each earthquake at that depth. The procedure was repeated for a range of depths and the resulting rms time residuals were plotted against the fixed depth. Such a plot must have a clear minimum and the depth which corresponds to this minimum should be the same as that calculated by the free solution. Fig. 5 shows that this is not always the case. There are two types of curves: type 1 curves have a clear rms minimum at a depth within the linearly predicted error of the depth found by the free solution. The depth of such an earthquake is well resolved. Curve type 2, however, is wider and sometimes shows (see curve 2, Fig. 5b) that the free solution locates the earthquake at a depth corresponding to a local minimum, missing the global minimum. It was generally found that well-recorded events in areas inside or up to 8 km outside the network had rms–depth curves of type 1, whereas poorly recorded events had broader curves of type 2, depicting poor depth resolution.

10 Aftershock locations: epicentres

In total, 1399 aftershocks were located and are shown in Fig. 6. East–west or north–south linear trends, passing near stations, occur for small and poorly recorded earthquakes, since the location program cannot resolve their longitude (or latitude) and holds it fixed.

Fig. 7 shows the epicentres of 600 events which were recorded by at least five stations, with at least one station reporting both *P*- and *S*-phases. Three distinct areas of activity can be seen separated by gaps. This epicentral distribution suggests that seismic slip occurred either along different sections of the same fault or along different faults. Such complicated seismic faulting at depth is supported by the complex pattern of surface faulting observed after the mainshock (Mercier *et al.* 1979). In view of this it was decided that only good quality locations would be considered for the final analysis.

The selection of the best locations were based on the results of the above location accuracy tests. The criteria for good locations were:

(1) events recorded by six or more stations, with at least two *S*-arrivals;
(2) events with errors in epicentre (ERH) and in depth (ERZ) < 2 km;
(3) events with rms residuals <0.15 s;
(4) events with at least one station at an epicentral distance smaller than their depth;
(5) events whose depth was not held fixed at 6 km (i.e. the starting depth in the computation).

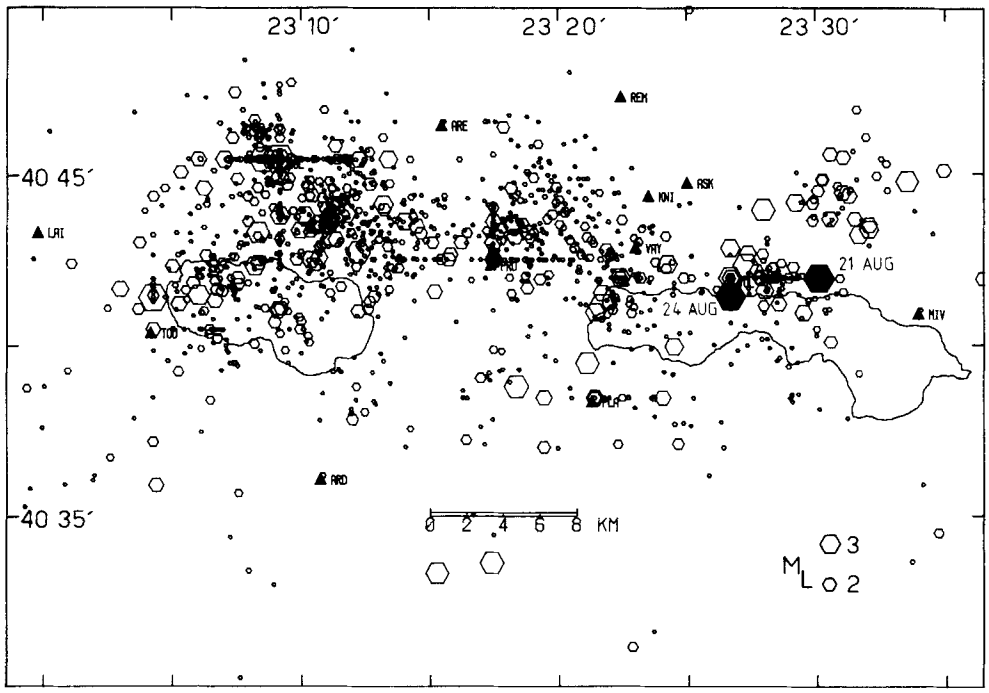

Figure 6. Epicentral distribution of all the located events. Filled triangles are recording stations. Not all these stations were operating simultaneously. The horizontal and vertical linear trends are small, poorly recorded shocks whose latitude or longitude is held fixed by the location program. The size of the hexagons increases with magnitude (see lower right corner of the figure).

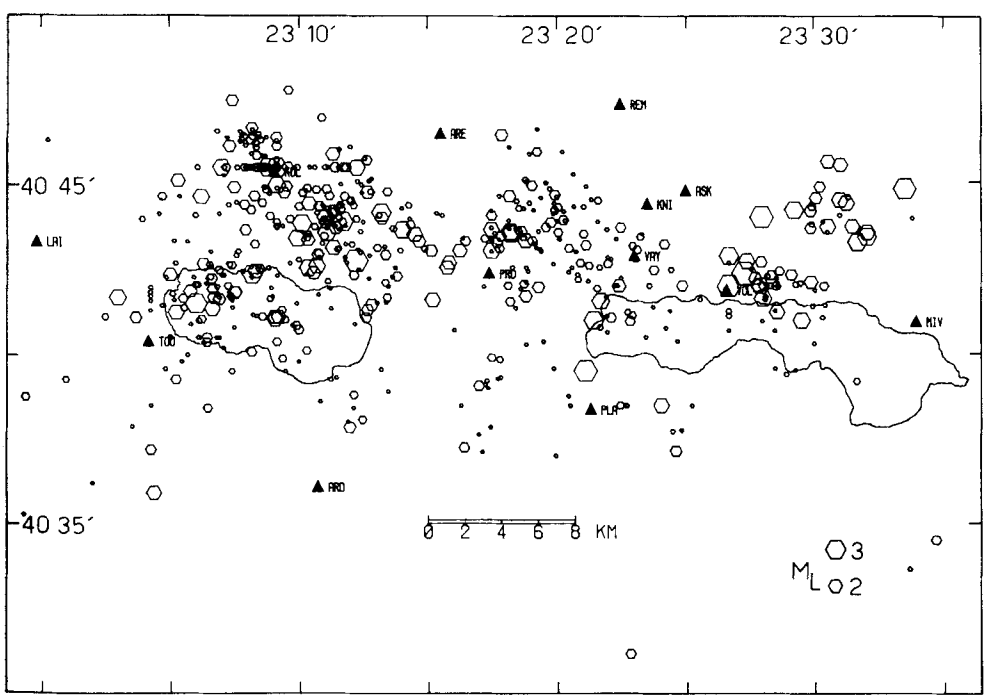

Figure 7. Epicentral distribution for the 600 events recorded by at least five stations, with at least one station reporting both *P*- and *S*-arrivals.

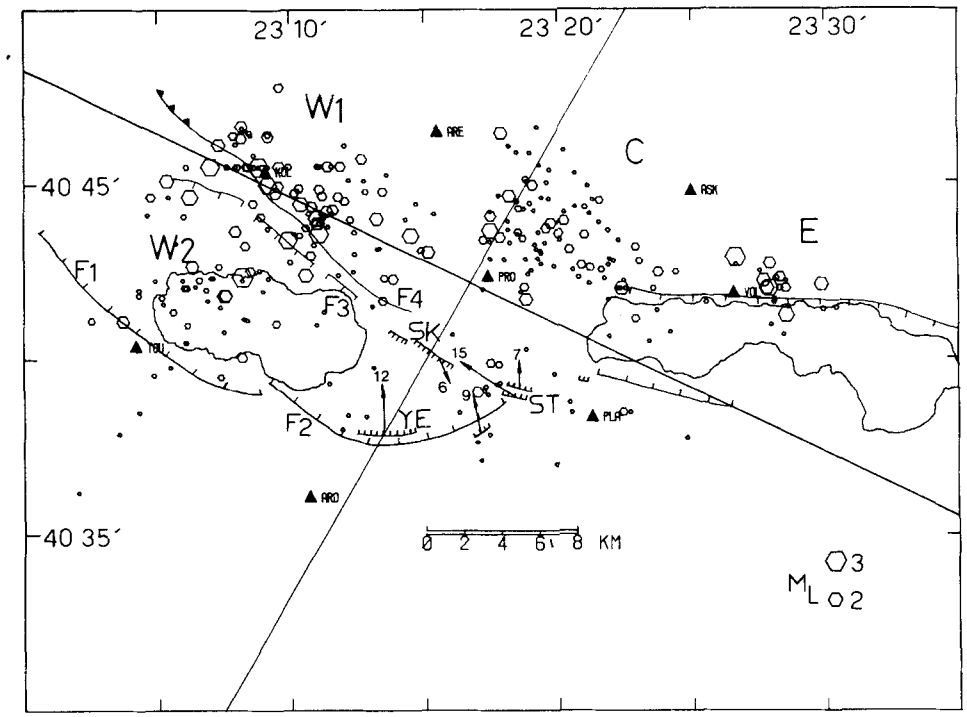

Figure 8. Epicentres of the 297 best located aftershocks. The main geological faults (normal or reverse) are from Kockel & Mollat (1977) and are marked F1–F4. The 1978 fault-breaks which are likely to be related to seismic movements at depth are shown as fault-segments densely hatched on the downthrown side. The slip-vectors are from Mercier *et al.* (1979) and the numbers near them denote average vertical displacement in centimetres. The stations shown as filled triangles were operating for most of the recording period. SK (Skolario), YE (Yerakarou) and ST (Stivos) are villages.

Based on these criteria 297 accurately located aftershocks were selected and are shown in Fig. 8. Their magnitudes (M_L) range between −1 and 3.8. This procedure has inevitably excluded from the final dataset some larger shocks for which *S*-phases were not clearly identifiable.

The following discussion is based solely on these high quality locations; the rest of the located events provide only a general view of the aftershock distribution.

The aftershocks are located to the north-east and north-west of the surface breaks. In the east all epicentres were to the north of the graben whereas in the west there was considerable activity within the boundaries of the graben. The epicentres shown in Fig. 8 show three distinct areas of activity similar to those of Fig. 7. These three areas are marked E (eastern), C (central) and W (western). Clearly defined gaps separate these three clusters. The western part can be further divided in two parts, W1 and W2.

11 Hypocentres

Fig. 9 shows two cross-sections of the seismic activity; one trending north-east is normal to the main north-west trend of the geological structures in the region, the other is parallel to this trend. The separation of the activity into three main parts is clear in Fig. 9 (bottom). A more detailed discussion of the hypocentral distribution of each region is given in the following sections. However, it is worth noting here that depths for the central and western

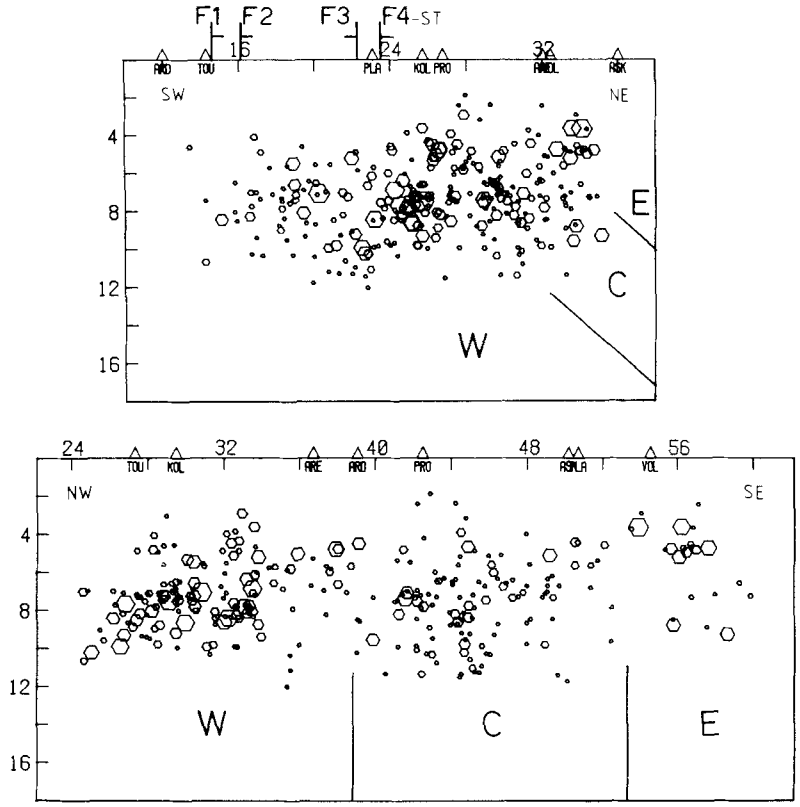

Figure 9. Two cross-sections trending north-east (upper) and north-west (lower) with no vertical exaggeration. Their positions are shown in Fig. 8. The scale is shown on the vertical axis in kilometres. The horizontal axis shows distance along the section. Faults are also shown as vertical bars, with a horizontal bar on the downthrown side. Open triangles are recording stations.

parts extended from 3 to 12 km, with a high concentration at 7–8 km (see also Fig. 10). By contrast, in the eastern part, most of the events were shallower than 6 km.

Some aftershocks appeared to be shallower than 3 km, but had depth errors larger than 2 km and so were excluded from the present dataset.

11.1 EASTERN PART

The eastern part of the activity (marked E in Figs 8 and 9) was an aftershock sequence on its own. It followed a magnitude $M_L = 4.2$ shock, on August 21, 89 days after the largest foreshock and 61 days after the mainshock. The epicentre of this earthquake along with that of its largest aftershock are shown in Fig. 6 as filled hexagons. However, no *S*-phases for either of these events could be recognized on the records and their depths were not well resolved, so they were both excluded from the high quality locations.

This smaller aftershock sequence is significant, since it enlarged the focal region of the earlier part of the 1978 sequence. As already mentioned, these events appear to be shallower than those in the other parts of the aftershock distribution. This depth difference is considered real because location tests with real and synthetic data showed that depth resolution is high in the vicinity of stations. However, in order to confirm this result and to check for false rms minima a further test was carried out. Selected earthquakes of the eastern sequence

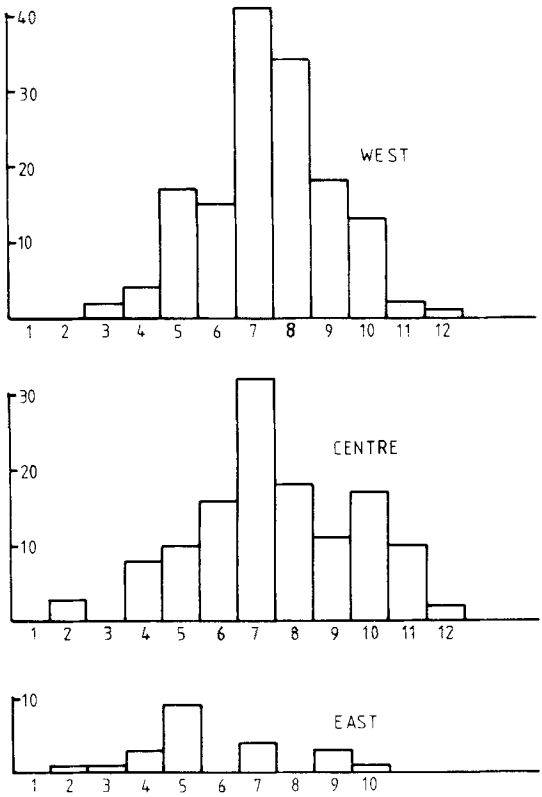

Figure 10. Depth histograms of the best locations in the three main parts of the aftershock distribution. Depths (horizontal axis) are in kilometres.

were located at fixed depths of 1–12 km. The depths which resulted in the minimum rms residuals were found to be shallower than 5 km and not significantly (i.e. within the 67 per cent level of significance) different from the depths of the free solution. This confirmed that the earthquakes in the eastern cluster were indeed shallower than those in other parts of the aftershock region. (In Fig. 7 another cluster of aftershocks can be seen north of the eastern activity. These earthquakes were not located accurately and are not included in Fig. 8. They occurred 10–15 days before the eastern activity discussed above but it is not clear how they relate to it.) Fig. 11 shows the positions of two cross-sections E1–E1′ and E2–E2′ and Fig. 12 shows the aftershocks projected on to these cross-sections. The small number of events limits any meaningful interpretation and it is not clear whether the activity is related to the east–west striking normal fault, downthrown to the south, which lies along the north edge of the lake.

11.2 CENTRAL PART

Fig. 13 shows two cross-sections of the central part of the activity. The positions of these two cross-sections are shown in Fig. 11. Cross-section C1–C1′ is normal to the apparent north-west trend of the activity and cross-section C2–C2′ normal to the strike of the fault plane, as deduced from the *P*-wave fault-plane solution of the mainshock on June 20 (Soufleris & Stewart 1981). In both cross-sections the hypocentres of the largest foreshocks and the mainshock are also shown.

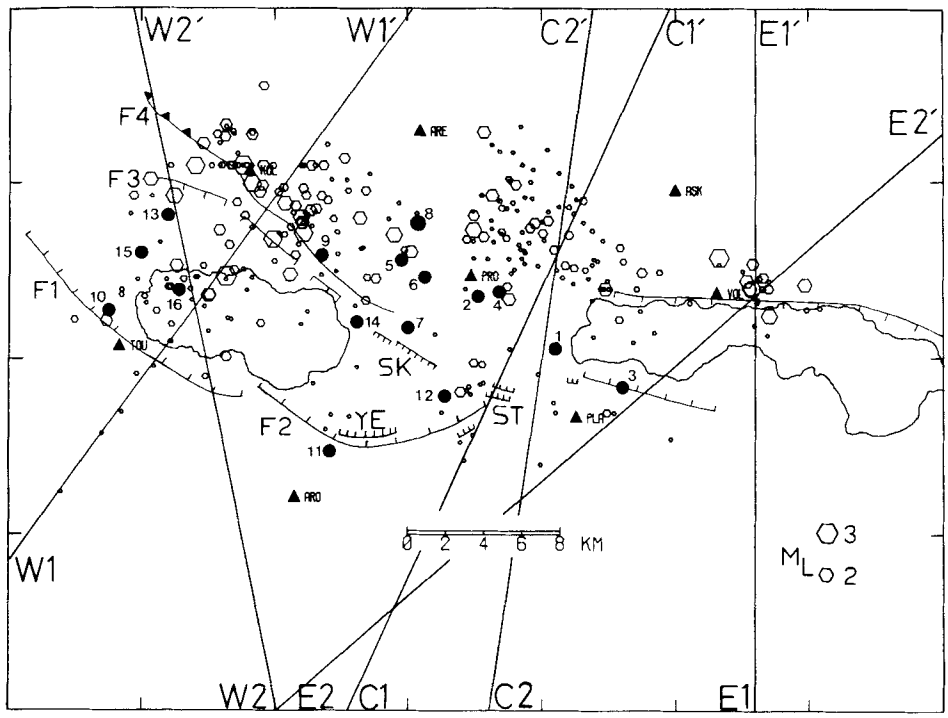

Figure 11. The same shocks as in Fig. 8, with the positions of six cross-sections shown. In addition, the epicentres of the 16 largest teleseismically recorded events of the sequence (Table 3) are shown as filled circles. The numbers of these events are the same as in Table 3.

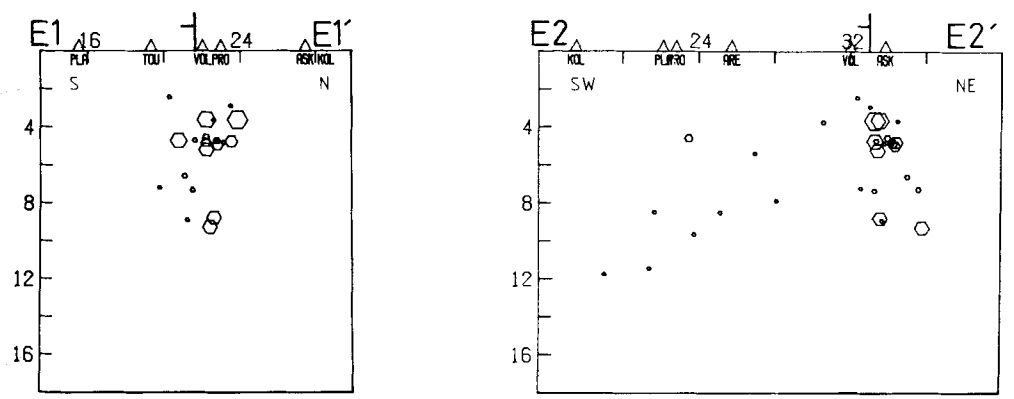

Figure 12. Two cross-sections for the eastern part of the activity. Rest as in Fig. 9.

A dense concentration of hypocentres defines a zone which dips by about 45° NE for both cross-sections and intersects the Earth's surface at the position of the surface break at Stivos, marked ST in Figs 11 and 13. The largest foreshock (number 2) and the mainshock (number 8), both of which have depths constrained to 6 ± 2 km by waveform modelling (Soufleris & Stewart 1981; Soufleris & King 1981), lie close to this dipping zone. The proximity of these locations, and the fault plane dips of 49° NNE and 46° NNE for these

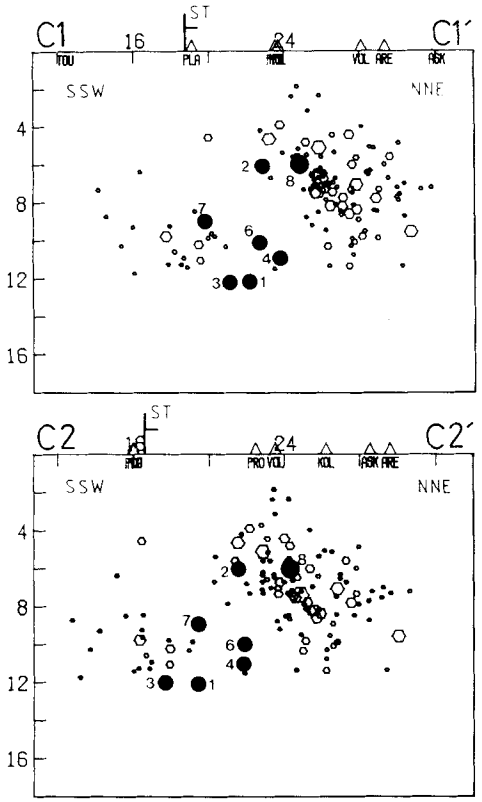

Figure 13. Two cross-sections for the central part of the activity. Cross-section C2–C2′ is normal to the strike of the fault-plane, as deduced from the *P*-wave fault-plane solution (Soufleris & Stewart 1981). The teleseismically recorded and relocated foreshocks and mainshock (from Table 3) are shown as filled circles. Note the proximity of events 2 (the largest foreshock, on May 23) and 8 (the mainshock, on June 20) to the dipping zone defined by the main cluster. Event 5 was located in the air and it is not shown. Rest as for Fig. 9.

two shocks, deduced from their fault plane solutions, suggests that they may both be associated with slip along the same fault, which reached the surface at Stivos. If this is so, there is significant activity above the fault, which presumably represents minor faulting and internal deformation of the downthrown block, caused either by non-uniform slip on the main fault or curvature of the fault plane itself.

The shocks directly below the surface break ST are deeper than most of the central activity and they do not appear to be related to the same fault (Fig. 13). The uncertainties in the hypocentres of the teleseismically recorded events in this group are greater than those of the locally recorded aftershocks, although some (e.g. number 6, Table 3) were recorded by a large number of stations and are expected to be accurate to within about 4 km. However, the microseismic activity clearly splits into two distinct groups, so it is quite possible that the teleseismic distinction is also real and that some of the foreshocks of the June 20 mainshock (notably number 6 of magnitude 5.3 on June 19) did not occur on the main Stivos fault.

11.3 WESTERN PART

Fig. 14 shows two cross-sections of the western part of the activity together with the hypocentres of the mainshock and the largest teleseismically recorded aftershocks. Here a more

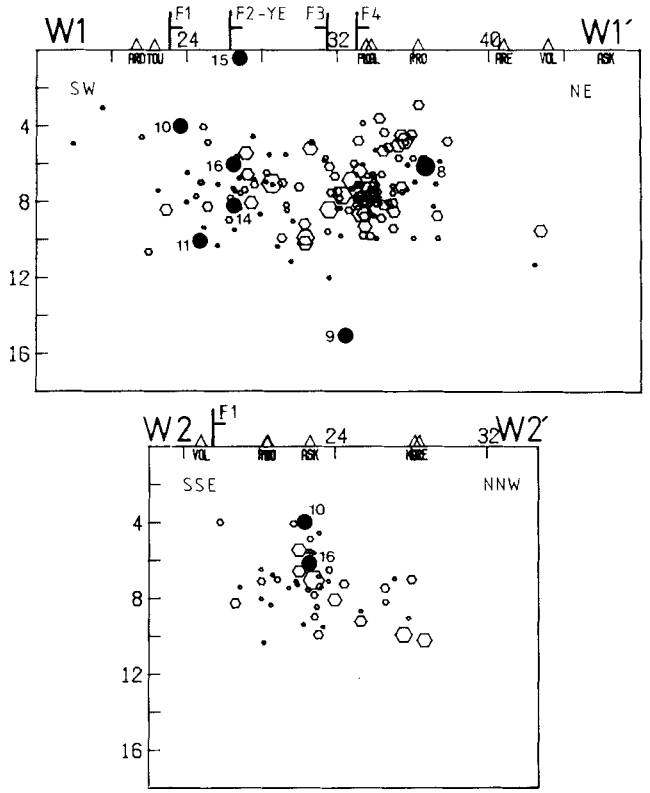

Figure 14. Two cross-sections for the western part of the activity along lines shown in Fig. 11. The teleseismically recorded and relocated mainshock and aftershocks (from Table 3) are shown as filled circles. Events 12 and 13 were located in the air and are not shown. Rest as for Fig. 9.

complicated pattern is seen, probably because more than one fault has been reactivated. In cross-section gaps divide the activity into three parts: the first consists of shallow earthquakes at depths between 2 and 6 km (below stations PLA and PRO, Fig. 14, top). It is difficult to establish whether this activity is associated with the reactivation of any of the nearby known faults. The second forms a tighter cluster, located at depths between 5 and 10 km, and contains most of the aftershocks in the western part. The third zone is a more diffuse pattern south-west of the main cluster. The aftershocks of the third zone are also projected on to another cross-section W2–W2′ (Fig. 14, bottom), normal to its apparent east-north-east trend (see Figs 11 and 7). The largest aftershock (event 16) also appears to be associated with this part of the activity. It is interesting that this cluster in map view defines a trend (see Figs 11 and 7) which intersects the fault F1 obliquely; there are no known faults with similar trends in that region.

12 Fault-plane solutions

During the recording period no more than eight stations were operating at one time and so in the optimum case no more than eight *P*-wave first-motions were available. This reduces the likelihood of well constrained fault-plane solutions, although in a few cases unique solutions could be obtained from only eight readings. In general, however, it was necessary to combine the data of more than one event in order to construct composite fault-plane solutions.

The basic assumption of a composite fault-plane solution is that the radiation pattern of all the considered events is the same. Under this assumption even a small number of recording stations can provide enough first-motion readings for an adequate coverage of the focal sphere, provided that these events are sufficiently far from each other. However, as first-motion readings of different events are combined, inconsistencies are introduced. The process of constructing a composite fault-plane solution is one of trial and error: fault-plane solutions for individual events are combined for a well-constrained focal mechanism, with as few inconsistent polarity readings as possible.

Initially, we constructed individual fault-plane solutions for each of the 297 best located aftershocks. Of these only four (nos 3, 12, 16 and 23 in Fig. 18) were well constrained and the rest were combined to construct composites. To do this, fault-plane solutions of 2–5 events, within well-defined clusters of 3 km^3 and consistent with each other, were overlayed and two nodal planes were drawn, as if the total number of polarity readings were from a single event. In this way 24 well-constrained solutions were obtained and they are shown in

Table 5. Data for the fault-plane solutions (individual or composite). The numbers in the first column are the same as in Figs 15, 17 and 18. The data of each composite fault-plane solution are shown in line with the location of the largest event of the group. This location is followed by the locations of the other events of the group.

No	Day Aug	O.Time	40° Lat.'	23° Lon.'	D.	1st pla Az.	1st pla Dip	2nd pla Az.	2nd pla Dip	P axis Az.	P axis Dip	T axis Az.	T axis Dip
1	01	152024	44.96	19.03	08	102	36	130	56	066	78	206	10
	09	124649	44.60	19.38	07								
	09	152917	45.04	19.57	06								
	18	203123	45.07	18.81	08								
2	02	103014	43.04	15.12	05	176	46	105	64	326	52	124	10
	10	055108	43.10	14.85	06								
3	06	042242	43.65	07.91	09	080	44	109	50	074	76	183	08
4	07	025346	43.66	17.47	07	115	46	115	44	015	89	015	01
	06	151853	43.39	17.21	05								
	07	025242	43.34	17.47	06								
	15	193208	43.47	17.83	08								
5	07	072652	45.49	07.00	08	086	46	109	46	096	90	007	01
	16	231117	46.12	07.31	09								
	16	232400	45.49	07.61	07								
6	07	094727	39.06	16.96	10	109	50	085	42	245	80	007	04
	07	094823	39.09	17.20	09								
	18	151955	39.89	17.47	10								
	18	181442	39.84	17.78	11								
	18	181624	39.27	17.70	11								
7	07	130916	44.22	11.33	08	066	54	181	60	118	51	123	04
	09	020751	44.15	11.14	08								
	09	234050	44.08	11.22	08								
8	08	223900	45.71	12.63	09	056	48	040	54	261	78	139	08
	11	110943	45.09	12.70	06								
	19	151204	44.78	12.76	06								
9	08	232531	43.57	11.05	07	104	66	211	30	138	64	003	20
	08	225653	43.87	11.01	06								
10	09	130406	39.55	04.83	05	071	42	066	48	297	82	152	08
	11	100313	39.77	05.47	07								
	23	172256	38.48	04.27	04								
11	09	160110	44.14	15.34	07	022	80	121	81	071	02	340	16
	07	053750	43.98	14.30	07								
12	10	053652	42.65	06.30	08	118	70	160	26	008	62	043	28
13	11	223142	42.29	13.79	05	142	30	209	64	005	70	217	18
	05	091050	41.66	13.41	07								
14	16	145740	42.52	08.47	10	079	42	102	54	064	80	183	10
	17	203543	42.53	08.81	08								
15	18	020905	42.26	06.57	07	076	66	131	42	060	60	009	14
	17	213203	41.97	06.83	08								
	20	011341	42.03	06.89	08								
	23	143356	41.67	06.88	07								
16	18	073545	41.09	02.49	11	074	52	101	40	110	76	355	06
17	18	100137	43.44	18.68	06	103	56	123	36	156	74	021	12
	09	062921	43.25	19.15	07								
	17	212513	43.08	19.34	07								
18	19	042557	44.97	09.14	09	101	48	107	42	115	88	014	02
	18	052129	45.49	09.14	07								
19	21	125815	42.34	08.17	07	075	40	075	50	345	85	165	05
	10	062931	42.25	08.16	06								
20	22	203537	46.38	07.85	09	093	50	208	44	124	78	016	08
	16	211748	46.13	07.93	07								
21	23	113411	44.85	11.10	05	098	30	058	68	297	62	161	22
	08	225517	44.65	11.17	04								
22	23	162242	44.65	18.16	07	115	68	115	22	205	68	025	22
	08	110459	44.29	18.52	10								
	09	145213	44.44	18.94	09								
	18	140140	44.23	19.08	11								
23	23	191353	41.82	07.54	07	083	62	110	30	141	70	002	14
24	28	041036	43.87	19.75	09	117	30	117	60	027	75	207	15
	08	213333	43.91	20.02	08								
	14	014317	43.94	20.23	08								

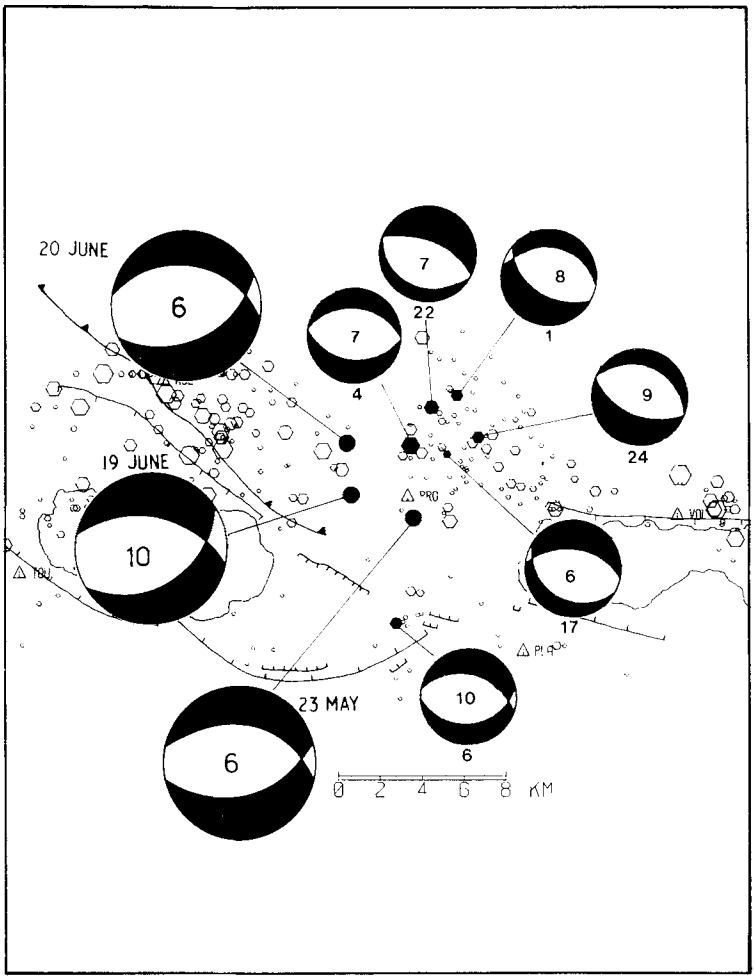

Figure 15. Aftershock epicentres and fault-plane solutions for the central part of the activity shown as equal area projections of their lower hemisphere. Numbers below the mechanisms identify events in Fig. 18 and Table 5. The balloons are connected to the location of the largest event of the group of each composite fault-plane solution. Numbers in the dilatational quadrants denote depth (in kilometres). The mechanisms of the two largest foreshocks (on May 23 and June 19) and the mainshock (on June 20), obtained from teleseismic data, are also shown.

Fig. 18. The orientation of the planes and other relevant data for each of these mechanisms are listed in Table 5.

12.1 CENTRAL PART

The eastern part of the aftershock activity occurred outside the network and all the stations plotted on one side of the focal sphere. It was thus not possible to obtain well-constrained fault-plane solutions for these earthquakes.

Fig. 15 shows five fault-plane solutions for the central part of the activity and one (no. 6) for the deeper cluster directly below the surface ruptures. All these mechanisms show normal faulting. The cross-sections C1–C1′ and C2–C2′ in Fig. 13 define the north-east dipping plane to be the fault-plane. Solution no. 6 also exhibits normal faulting and the cross-sections in Fig. 13 show that it occurred on a different fault, though it is difficult to determine which is the fault-plane in this case.

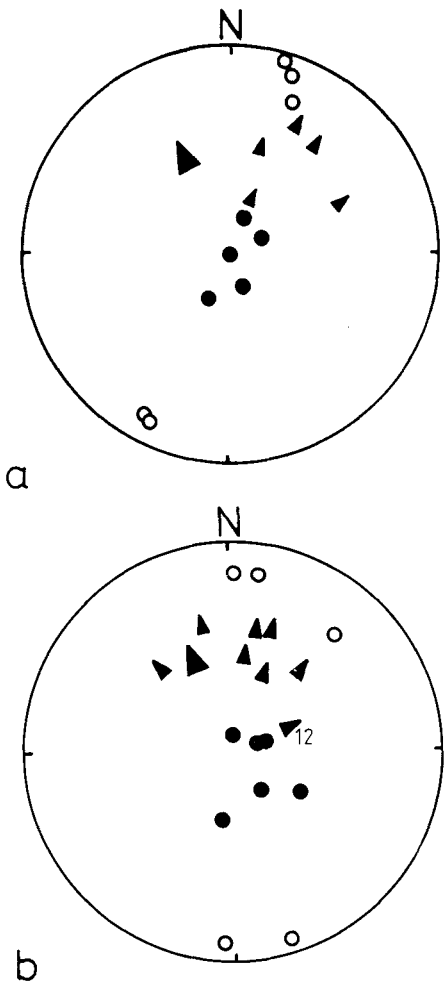

Figure 16. *P*-axes (closed circles), *T*-axes (open circles) and slip-vectors (smaller arrows) for the fault-plane solutions in the central part (top) and the W2 part (bottom) of the aftershock distribution. The mean slip-vector for the two largest teleseismically recorded foreshocks and the mainshock are also shown as larger arrows.

It is worth noting that none of the five fault-plane solutions of the central cluster exhibit the left-lateral component shown by the three largest events of the sequence, whose mechanisms were determined from teleseismic data (Fig. 15). The mean azimuth of the slip-vector for the fault-plane solutions of the central cluster is N 30°. This azimuth differs by about 60° from the mean azimuth of the slip-vector for the teleseismically determined focal mechanisms (Fig. 16a). The difference, viewed together with the hypocentres of the larger (teleseismically located) events at the western end of the fault segment suggests that, as far as the central part of the activity is concerned, the onset of slip occurred at its western edge and had a small left-lateral component. In later stages, as the slip extended towards the eastern part of the fault, it was mainly confined to pure dip-slip motion.

12.2 WESTERN PART

Fig. 17 shows the fault-plane solutions for the western part of the activity along with the solution for the mainshock on June 20. Here again normal faulting is predominant but a

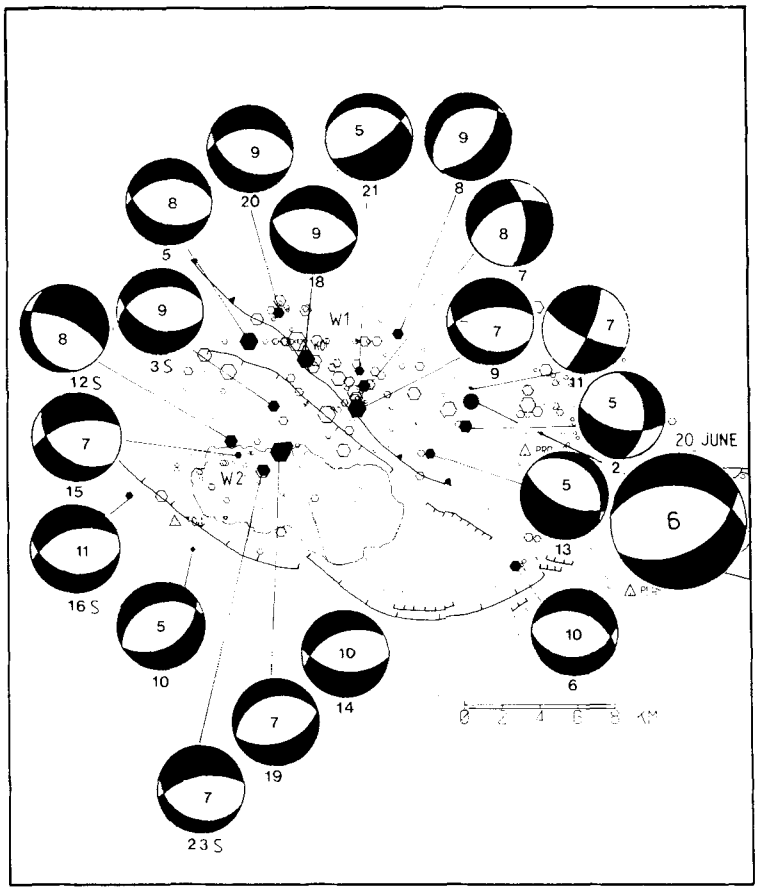

Figure 17. As for Fig. 15 but for the western part of the activity. An S after the event number denotes a fault plane solution for a single shock.

more complicated pattern emerges. The activity can be further divided into two parts, W1 and W2 (Fig. 17).

The south-western part (part W2 in Fig. 17) exhibits more consistent focal mechanisms, with the exception of mechanisms no. 12. Cross-section W2–W2′ (Fig. 14, bottom) suggests that the north-north-west dipping plane may be the fault-plane. Fig. 16 (bottom) shows a compilation of the directions of *P*- and *T*-axes and the slip-vectors for mechanisms of this cluster. These slip-vectors show a considerable scatter with a mean azimuth of N 9°.

Focal mechanisms 5, 18 and 20 have both their nodal planes subparallel to the north-west trend of the major faults in the region and their north-east dipping planes may be their fault-planes. Further east, solutions 2, 7, 8, 9 and 21 exhibit anomalous patterns. It is interesting, however, that focal mechanism 11 shows strike-slip motion. If its north-north-east striking plane is its fault-plane then this mechanism is consistent with right-lateral slip of the western block with respect to the quiescent area which separates the central from the western part of the activity.

In general, within the northern part of the western aftershock cluster there is a large variety of focal mechanisms reflecting a more complicated mode of seismic deformation. Such complex style of deformation is not unusual for aftershock sequences of large normal-faulting events (Pitt, Weaver & Spence 1979; Arabasz, Richins & Lauger 1981).

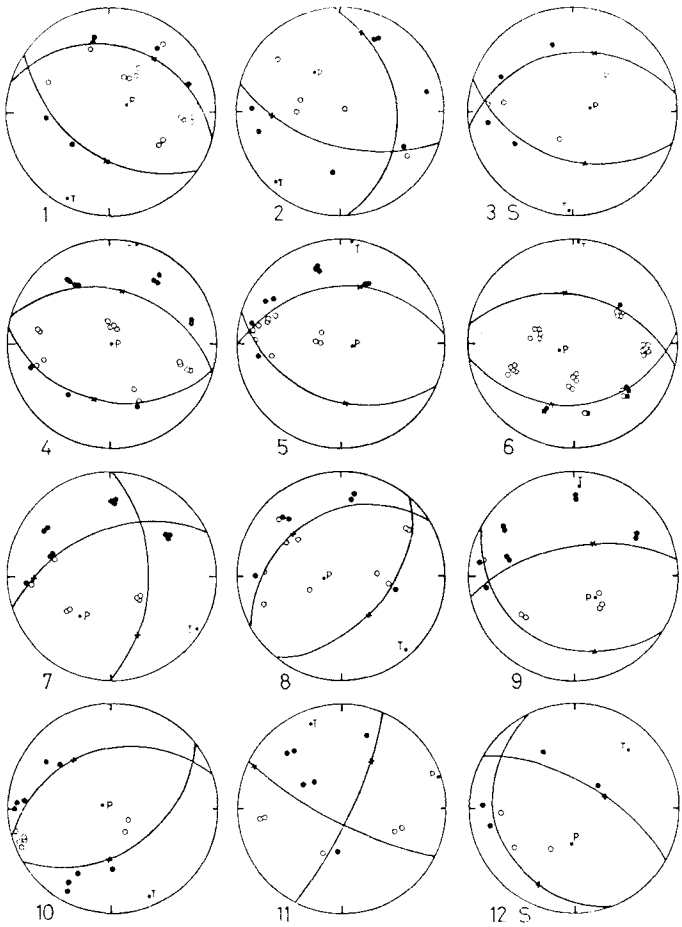

Figure 18. Polarity readings for the single (denoted by an S after their number) and the composite fault-plane solutions shown in equal area projections of their lower focal hemisphere. Open circles denote dilatations, closed compressions. Numbers below each solution identify events in Table 5.

13 Source dimensions and fault parameters

The data discussed so far, combined with information obtained from waveform analysis (Soufleris & Stewart 1981; Soufleris & King 1981) may be used to investigate the likely source dimensions, slip amplitudes and strain changes associated with the two largest events of May 23 and June 20.

Let us initially assume that the fault area which ruptured during the mainshock of June 20 is defined by the total area covered by the central and western parts of the aftershock distribution. (The eastern part of the aftershock activity, discussed earlier, was a separate sequence associated with an event two months after the mainshock.) The mean seismic slip is given by:

$$\bar{u} = \frac{\mathcal{M}_0}{A}$$

where A is the fault area and $\mathcal{M}_0$ is the geometric moment (King 1978; Kanamori & Anderson 1975) which is related to the commonly quoted moment M_0 by the shear modulus, μ:

$$\mu \mathcal{M}_0 = M_0.$$

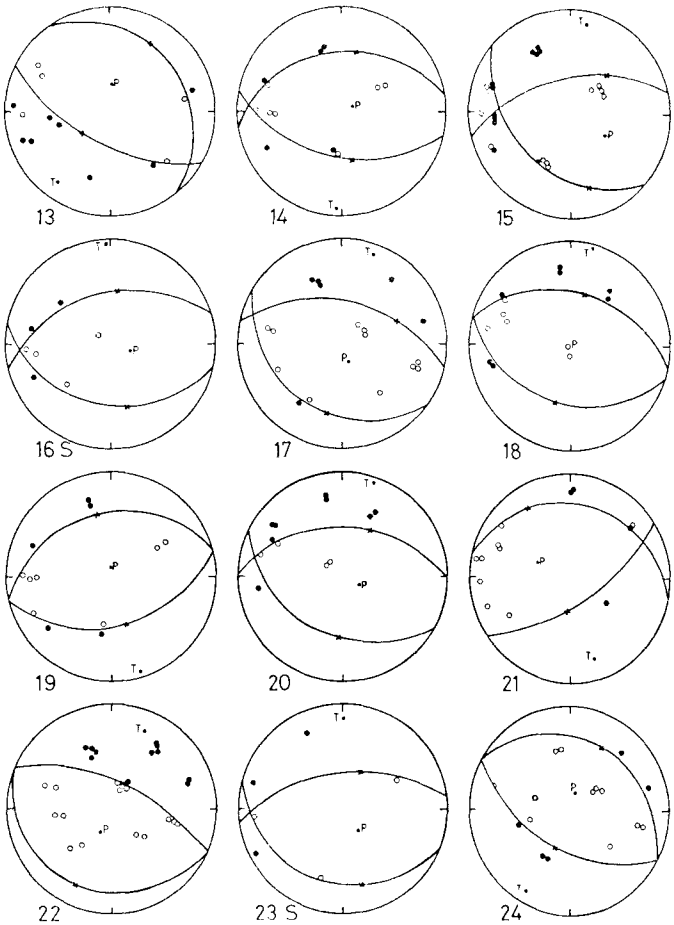

Figure 18 – *continued*

For a value of M_0 of 5.2×10^{25} dyne cm ($\mathcal{M}_0 = 1.75 \times 10^8 \text{m}^3$, with $\mu = 3 \times 10^{11}$ dyne cm^{-2}) from Soufleris & Stewart (1981) and a fault area of 28×17 km^2 (assuming a fault length of 28 km and a down-dip width of 17 km from the aftershock locations) the mean displacement is 37 cm. Using these estimates the strain drop Δe, can be obtained from

$$\Delta e = \frac{C\bar{u}}{L}$$

where L is the shortest fault dimension and C is a non-dimensional shape factor. Shape factors have been calculated for circular and rectangular fault geometries which are either buried or intersect the surface (e.g. Kanamori & Anderson 1975). The present fault is apparently rectangular but only partially breaks the surface (with a 12 cm mean observable offset) and thus none of these geometries is directly applicable. However the shape factor is near unity for all geometries and does not vary by a factor of more than about 2. Thus the strain drop is approximately 2.1×10^{-5}, which may be interpreted as a static stress drop of 6.3 bar.

The errors in these estimates are caused mainly by the shape factor assumption, errors in the estimate of M_0, or in appropriately interpreting the significance of the aftershock region. Although the moment is averaged over a large number of stations (Soufleris & Stewart 1981)

it is still uncertain by a factor of 3. Little can be done about this, although the assumption that the mainshock fault area is $17 \times 8\,km^2$ may be questioned. A down-dip length of 17 km is the maximum likely and may be an overestimate as it assumes that the rupture reached the surface, where faulting was small and discontinuous. Moreover it is possible that some of the aftershock area is related to movement in the foreshock of May 23. This possibility is discussed below.

The foreshock of May 23 was smaller than the mainshock with $m_b = 5.7$, $M_0 = 5.6 \times 10^{24}$ dyne cm, $\mathcal{M}_0 = 1.9 \times 10^7 m^3$ (Soufleris & King 1981) and can be considered as a square fault bounded by the medium (a circular fault gives a similar result). If it is assumed to have the same displacement to length ratio (or the same static stress drop) as the main event then the fault width, L, is obtained from:

$$L = \left(\frac{C.\mathcal{M}_0}{\Delta e}\right)^{1/3}$$

which gives a value of 9.7 km, if C is taken to be unity and Δe to be 2.1×10^{-5} as found earlier. This in turn gives a mean displacement of 20 cm. The length of 12 km and down-dip width of 17 km of the area defined by the central part of the aftershock distribution is in reasonable agreement with this estimate, especially since a down-dip width of 17 km is the maximum likely and assumes that the faulting reached the surface, which it scarcely did.

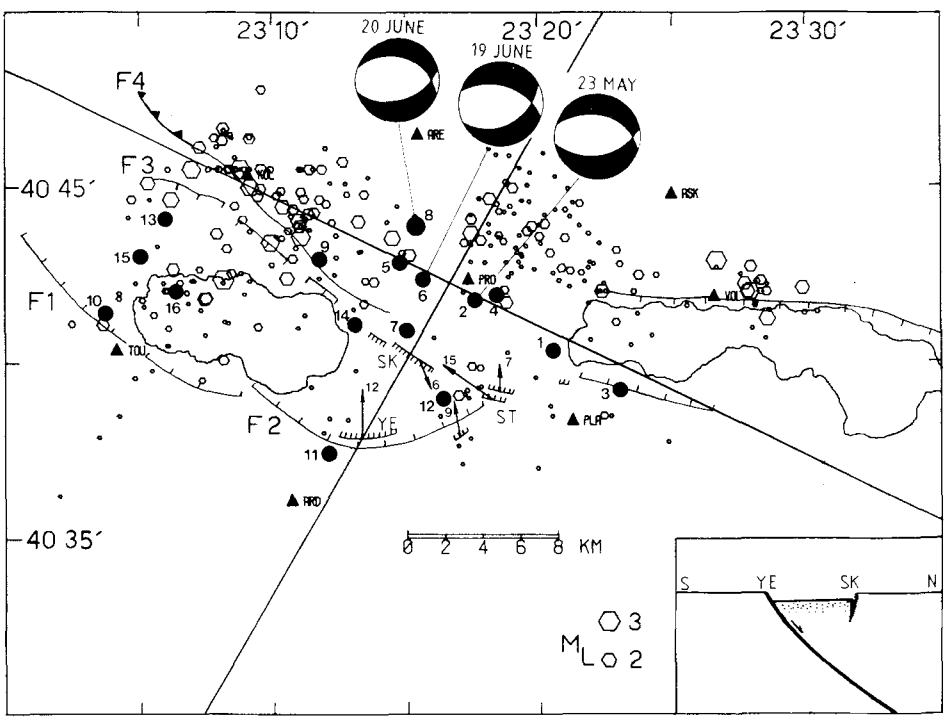

Figure 19. Epicentres of the 297 best located aftershocks are shown along with those of the 16 largest teleseismically recorded (filled circles, from Table 3) events of the sequence and the three fault-plane solutions from Soufleris & Stewart (1981). Event 2 is the largest foreshock, on May 23 ($m_b = 5.7$), event 8 is the mainshock, on June 20 ($m_b = 6.1$) and event 16 is the largest aftershock, on July 4 ($m_b = 5.1$). The numbers of the larger events are sequential in time. Numbers near the slip-vectors denote average vertical displacement in centimetres. Inset shows a cartoon section of the faulting.

Table 6. Summary of fault parameters.

	Moment		Rupture area (km^2)	$\bar{u}$ (cm)	Strain drop	Static stress drop (bar)
	$\mathcal{M}_0$ (m^3)	M_0 (dyne cm)				
June 20 (bilateral rupture)	1.75×10^8	5.2×10^{25}	28×17	36	2.1×10^{-5}	6.3
June 20 (unilateral rupture)	1.75×10^8	5.2×10^{25}	16×17	64	4.0×10^{-5}	12
May 23 (for bilateral June 20 shock)	1.9×10^7	5.6×10^{24}	9.7×9.7	20	2.1×10^{-5}	6.3
May 23 (for unilateral June 20 shock)	1.9×10^7	5.6×10^{24}	7.8×7.8	31	4.0×10^{-5}	12

This agreement, together with the epicentral position of the May 23 foreshock, suggests that the focal region of this event was only the area east of the mainshock location. This is supported by the positions of shocks 3 and 4 on May 24 (Fig. 19).

Although it is not clear whether both fault segments, west and east of the mainshock location, ruptured during that earthquake (in a bilateral fashion), it is tempting to suggest that only the western fault segment ruptured (unilaterally). The lack of substantial teleseismically recorded aftershock activity east of the mainshock location supports this suggestion. In this case the length of faulting during the mainshock was only 16 km. The new fault length would yield a displacement of 64 cm, which in turn results in a strain drop of 4×10^{-5} and a static stress drop of 12 bar. If this new strain drop were used to recalculate the mean displacement of the May 23 shock, an increased value of 31 cm would be obtained, with a fault dimension of 7.8 km.

The source parameters of the largest foreshock and aftershock are summarized in Table 6 on the assumption that the mainshock propagated either bilaterally east and west or only unilaterally to the west.

There are no reliable measurements of surface displacements following the foreshock of May 23. Local inhabitants, however, recollect that a crack with the north block downthrown appeared immediately after that event at Stivos (marked ST in Fig. 19). The same displacement was enhanced at the time of the mainshock, on June 20. This information suggests that the whole or part of the fault-segment that moved during the largest foreshock, on May 23, moved also during mainshock on June 20.

Kulhanek & Meyer (1979, 1981) used Brune's (1970, 1971) model as applied by Hanks & Wyss (1972) and calculated the source parameters for the mainshock from the *P*-wave spectra of five WWSSN stations. They found the moment to be 6.6×10^{25} dyne cm, a static stress-drop of 6.6 bar and a mean displacement of 27 cm. Their fault length estimate of 32 km is compatible with the length of 28 km suggested by the aftershock distribution, if both the western and the central aftershock clusters are taken to represent the area of faulting during the mainshock. However, if only the western cluster is considered to represent the mainshock fault area then their value overestimates the length of faulting by 100 per cent. Such an overestimate is expected because they did not correct their spectra for the effect of the free surface. The surface reflections *pP* and *sP* affect the *P*-wave spectra of shallow earthquakes and may result in wrong estimates of the corner frequency if their effect is not taken into account (Langston 1978).

14 The Thessaloniki sequence: a triple event

During the Thessaloniki sequence a series of earthquakes occurred along three different but adjacent fault segments. Using conventional terminology the series would be described as a complete sequence, of foreshocks (the largest being on May 23), mainshock (on June 20) and aftershocks (the largest on July 4). However, because the two largest events of the series and the smaller sequence to the east occurred on three different fault segments, the sequence can be described as a triple event (Das & Scholz 1981). It had three mainshocks, the first on May 23, the second on June 20 and the third on August 21. Each one of them was preceded by its own foreshocks and followed by its own aftershocks. The three mainshocks are hereafter called 'Event 1', 'Event 2' and 'Event 3'. The event sequence, therefore, occurred as follows: The foreshock activity of Event 1 started in early May (foreshock no. 1 being its largest foreshock, see Figs 19 and 20) and culminated on May 23, with the first mainshock of magnitude m_b =5.7. This earthquake ruptured only the fault area as defined by the central part of the aftershock distribution (Fig. 19). The mainshock was followed by its aftershocks (shock nos 3, 4 and probably 5 being the largest). The high stress concentration induced by this earthquake at the two ends of its fault zone was later released seismically. Shock nos 5, 6 and 7 were the largest foreshocks of Event 2, which occurred on June 20 (event no. 8 in Figs 19 and 20) and probably ruptured more than one fault segment in the western part of the aftershock area. The second mainshock was larger than the first and it was followed by its own aftershocks (shock nos 9, 10, 11, 12, 13, 14, 15 and 16 being the largest).

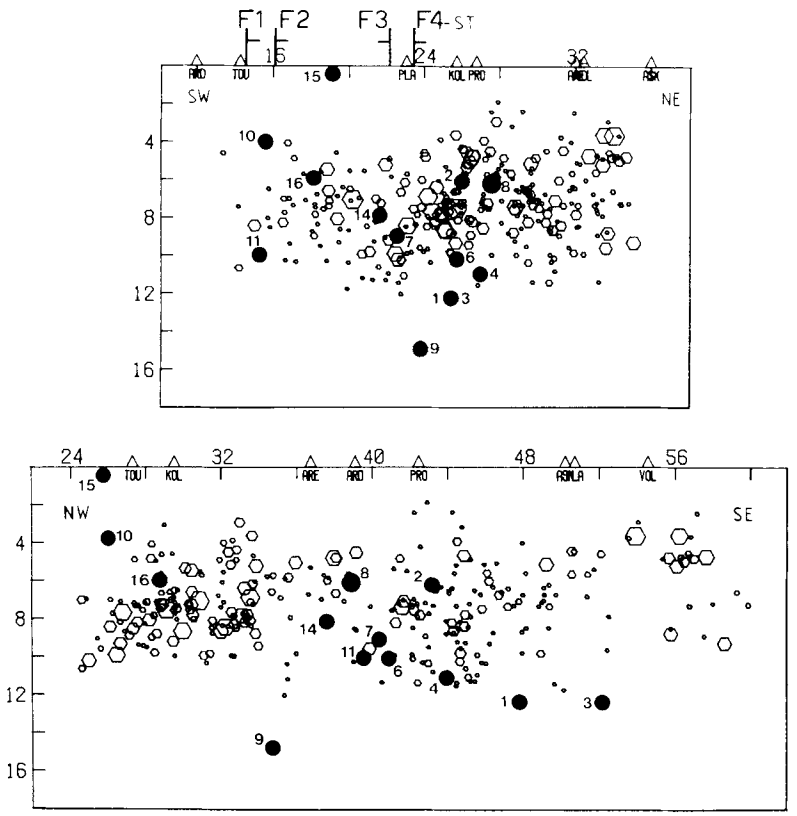

Figure 20. Two cross-sections (shown in Fig. 19) for all the earthquakes in Fig. 19. Events 5, 12 and 13 are located in the air and are not shown.

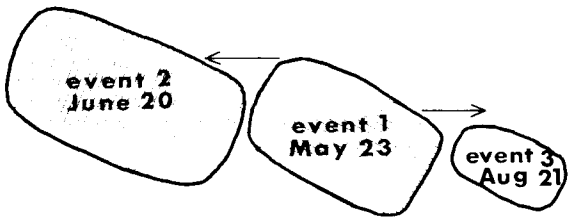

Figure 21. A cartoon showing the source regions for the three shocks of the triple event sequence.

A similar process of stress accumulation due to the movement of the central fault segment caused the smaller earthquake sequence to the east, 89 days after Event 1 and 61 days after Event 2. The source region for that smaller sequence is defined by the eastern part of the aftershock distribution (Fig. 19). Fig. 21 shows a cartoon of the geometry of faulting during the entire sequence.

Acknowledgments

Many fruitful discussions with Manuel Berberian and Dan McKenzie are much appreciated. Steve Roecker wrote an initial version of the program for the calculation of location errors due to the network configuration and Graham Yielding digitized half of the aftershock data.

The smoked-drum recorders were on loan from the Lamont-Doherty Geological Observatory, the Geophysical Laboratory of the University of Thessaloniki and Imperial College, London.

This research was supported by the Natural Environment Research Council and The Royal Society of London. CS gratefully acknowledges scholarships from IKY (Greece) and the British Council. The authors would particularly like to thank Professor Papazachos and other members of the Geophysical Laboratory of the University of Thessaloniki for the extensive help that they offered in this project.

Contribution No. 131, Department of Earth Sciences, University of Cambridge, Cambridge, UK.

References

Aki, K. & Lee, W. H. K., 1976. Determination of 3-D velocity anomolies under a seismic array using P arrival times from local earthquakes: 1. A homogeneous initial model, *J. geophys. Res.*, **81**, 4381–4399.

Arabasz, W. J., Richins, W. D. & Langer, C. J., 1981. The Pocatello Valley (Idaho–Utah border) earthquake sequence of March–April 1975, *Bull. seism. Soc. Am.*, in press.

Brune, J. N., 1970. Tectonic stress and the spectra of seismic shear waves from earthquakes, *J. geophys. Res.*, **75**, 4997–5009.

Brune, J. N., 1971. Correction to: 'Tectonic stress and the spectra of seismic waves from earthquakes', *J. geophys. Res.*, **76**, 5002.

Carver, D. & Bollinger, G. A., 1981. Aftershocks of the June 20, 1978 Greece earthquake: a multimode faulting sequence, *Tectonophys.*, **73**, 343–363.

Comninakis, P. E. & Papazachos, B. C., 1979. Distribution of macroseismic effects of the 1978 two major earthquakes in the Thessaloniki area of Northern Greece, *Publ. No. 11*, Geophysical Laboratory, Aristotelian University of Thessaloniki.

Crosson, R. S., 1976. Crustal structure modelling of earthquake data: 1. Simultaneous least squares estimation of hypocentre and velocity parameters, *J. geophys. Res.*, **81**, 3036–3046.

Das, S. & Scholz, C. H., 1981. Theory of time dependent rupture in the earth, *J. geophys. Res.*, **86**, 6039–6051.

Ellsworth, W. L. & Roecker, S. W., 1982. Sensitivity of the earthquake location problem to network geometry, *Geophys. J. R. astr. Soc.*, submitted.

Hanks, T. C. & Wyss, M., 1972. The use of body-wave spectra in the determination of seismic-source parameters, *Bull. seism. Soc. Am.*, **62**, 561–589.

Jackson, J. A., 1980. Errors in focal depth determination and the depth of seismicity in Iran and Turkey, *Geophys. J. R. astr. Soc.*, **61**, 285–301.

Jackson, J. A. & Fitch, T. J., 1979. Seismotectonic implications of relocated aftershock sequences in Iran and Turkey, *Geophys. J. R. astr. Soc.*, **57**, 209–229.

Jeffreys, H., 1961. *Theory of Probability*, Oxford University Press.

Kanamori, H. & Anderson, D. L., 1975. Theoretical basis of some empirical relations in seismology, *Bull. seism. Soc. Am.*, **65**, 1073–1095.

King, G. C. P., 1978. Geological faults: fracture, creep and strain, *Phil. Trans. R. Soc. A*, **288**, 197–212.

Kockel, F. & Mollat, H., 1977. *Geologischen karte der Chalkidhiki und Angrenzender Gebiete, 1:100,000* (Nord Griechenland).

Kulhanek, O. & Meyer, K., 1979. Source parameters of the Volvi-Langadhas earthquake of June 20 1978 deduced from body-wave spectra at stations UPPSALA and KIRUNA, *Bull. seism. Soc. Am.*, **69**, 1289–1294.

Kulhanek, O. & Meyer, K., 1981. Spectral study of the June 20, 1978 Thessaloniki earthquake, in *The Thessaloniki 1978 Earthquakes*, eds Papazachos, B. C. & Carydis, P., in press.

Langson, C. A., 1978. Moments, corner frequencies and the free surface, *J. geophys. Res.*, **83**, 3422–3426.

Lee, W. H. K. & Lahr, J. C., 1975. HYP071 (Revised): a computer program for determining hypocentre, magnitude and first motion pattern of local earthquakes, *U.S.G.S. Open File Rep. 75–311.*

Lilwall, R. C. & Francis, T. J. G., 1978. Hypocentral resolution of small ocean bottom seismic networks, *Geophys. J. R. astr. Soc.*, **54**, 721–728.

McKenzie, D., 1978. Active tectonics of the Alpine Himalayan belt: the Aegean sea and surrounding regions, *Geophys. J. R. astr. Soc.*, **55**, 217–254.

Makris, J. & Möller, L., 1977. Geophysical studies of the Chalkidiki ophiolites and their tectonic implications, in *VI Colloquium on the Geology of the Aegean Region*, pp. 623–643, ed. Kallergis, G., Möller Institute of Geological and Mining Research, Athens.

Mercier, J. L., Mouyaris, N., Simeakis, C., Roundoyannis, T. & Angelidhis, C., 1979. Intraplate deformation: a quantative study of the faults activated by the 1978 Thessaloniki earthquakes, *Nature*, **278**, 45–48.

Peters, D. C. & Crosson, R. S., 1972. Application of prediction analysis to hypocentre determination using a local array, *Bull. seism. Soc. Am.*, **62**, 775–788.

Pitt, A. M., Weaver, C. S. & Spence, W., 1979. The Yellowstone Park earthquake of June 30, 1975, *Bull. seism. Soc. Am.*, **69**, 187–205.

Soufleris, C. & King, G. C. P., 1981. A source study of the largest foreshock (on May 23) and the mainshock (on June 20) of the Thessaloniki 1978 sequence, in *The Thessaloniki 1978 Earthquakes*, eds Papazachos, B. C. & Carydis, P., Department of Earth Science, Thessaloniki University, Greece.

Soufleris, C. & Stewart, G. S., 1981. A source study of the Thessaloniki (northern Greece) 1978 earthquake sequence, *Geophys. J. R. astr. Soc.*, **67**, 343–358.